

Non-Convex Weighted ℓ_p Nuclear Norm based ADMM Framework for Image Restoration

Zhiyuan Zha^a, Xinggan Zhang^a, Yu Wu^a, Qiong Wang^a, Lan Tang^{a,b}

^a School of Electronic Science and Engineering, Nanjing University, Nanjing 210023, China.

^b National Mobile Commun. Research Lab., Southeast University, Nanjing 210023, China.

Abstract

Since the matrix formed by nonlocal similar patches in a natural image is of low rank, the nuclear norm minimization (NNM) has been widely used in various image processing studies. Nonetheless, nuclear norm based convex surrogate of the rank function usually over-shrinks the rank components and makes different components equally, and thus may produce a result far from the optimum. To alleviate the above-mentioned limitations of the nuclear norm, in this paper we propose a new method for image restoration via the non-convex weighted ℓ_p nuclear norm minimization (NCW-NNM), which is able to more accurately enforce the image structural sparsity and self-similarity simultaneously. To make the proposed model tractable and robust, the alternative direction multiplier method (ADMM) is adopted to solve the associated non-convex minimization problem. Experimental results on various types of image restoration problems, including image deblurring, image inpainting and image compressive sensing (CS) recovery, demonstrate that the proposed method outperforms many current state-of-the-art methods in both the objective and the perceptual qualities. *Keywords:* Image restoration, low rank, nuclear norm minimization, weighted ℓ_p nuclear norm, ADMM.

^{*}Fully documented templates are available in the elsarticle package on CTAN.

1. Introduction

Image restoration (IR) aims to reconstruct a high quality image \mathbf{X} from its degraded observation \mathbf{Y} , which can be generally expressed as

$$\mathbf{Y} = \mathbf{H}\mathbf{X} + \boldsymbol{\eta} \quad (1)$$

where \mathbf{H} is a non-invertible linear degradation operator and $\boldsymbol{\eta}$ is the vector of some independent Gaussian white noise. With different settings of matrix \mathbf{H} , various IR problems can be derived from Eq. (1), such as image denoising [1, 2, 3, 4, 70] when \mathbf{H} is an identity matrix, image deblurring [5, 6, 7, 8] when \mathbf{H} is a blur operator, image inpainting [9, 10, 11, 12] when \mathbf{H} is a mask and image compressive sensing (CS) recovery when \mathbf{H} is a random projection matrix [13, 14, 15, 16]. In this work, we focus on the latter three problems.

IR is a typical ill-posed problem. To deal with this issue, image prior knowledge is usually exploited for regularizing the solution to the following minimization,

$$\hat{\mathbf{X}} = \arg \min_{\mathbf{X}} \frac{1}{2} \|\mathbf{Y} - \mathbf{H}\mathbf{X}\|_2^2 + \lambda \mathbf{R}(\mathbf{X}) \quad (2)$$

where the first term above is the data fidelity term and the second term depends on the employed image priors, and λ is the regularization parameter. Due to the ill-posed nature of IR, the image prior knowledge plays a critical role in enhancing the performance of IR algorithms. In other words, how to design an effective regularization model to represent the image priors is vital for IR tasks.

The classical regularization models, such as Tikhonov regularization [17] and total variation (TV) regularization [18, 19], exploited the image local structure and high effectiveness to preserve image edges. Nonetheless, they tended to over-smooth the image and some image details are usually lost.

As an emerging machine learning technique, sparse representation based modeling has been proved to be a promising model for image restoration [20, 21, 22, 23]. It assumes that image/image patch can be precisely represented as a sparse linear combination of basic elements. These elements, called atoms, compose a dictionary [20, 21, 24, 25]. The dictionary is usually learned from a

natural image dataset [20, 21]. The well known dictionary learning (DL) based methods, such as KSVD [20, 21], ODL [24] and task driven DL [25], have been
25 proposed and applied to image restoration and other image processing tasks.

Image patches that have similar pattern can be spatially far from each other and thus can be collected in the whole image. This so-called nonlocal self-similarity (NSS) prior is the most outstanding priors for image restoration. The seminal work of nonlocal means (NLM) [1] exploited the NSS prior to perform
30 a series of the weighted filtering for image denoising. Due to its effectiveness, a large amount of related developments have been proposed [3, 7, 16, 26, 27, 28, 29]. For instance, BM3D [28] exploited nonlocal similar 2D image patches and 3D transform domain collaborative filtering. Marial *et al.* [3] considered the idea of NSS by simultaneous sparse coding (SSC). Dong *et al.* [26] pro-
35 posed the nonlocally centralized sparse representation (NCSR) model for image restoration, which obtained the estimation of the sparse coding coefficients of the original image by the principle of NLM [1], and then according to those estimates, NCSR, centralized the sparse coding coefficients of the observed image to improve the restoration performance. Zhang *et al.* [29] proposed a group-based
40 sparse representation framework for image restoration.

Recently, image priors based on NSS [1, 4, 6, 7, 22, 26, 27, 28, 29, 30] and low-rank matrix approximation (LRMA) [43, 31, 32, 39, 33, 34] have achieved a great success in IR [35, 36, 37]. A flurry of IR have been proposed, such as image alignment [35], image/video denoising [4, 36, 38], image deblurring
45 [6, 40, 41] and image inpainting [9, 42]. However, these methods usually suffer from a common drawback that the nuclear norm is usually adopted as a convex surrogate of the rank. Despite a good theoretical guarantee by the singular value thresholding (SVT) model [43], the nuclear norm minimization (NNM) [43, 31, 33] tends to over-shrink the rank components and treats the different
50 rank components equally, and thus it cannot approximate the matrix rank accurately enough. To enforce the low rank regularization efficiently, inspired by the success of ℓ_p ($0 < p < 1$) sparse optimization [44, 45, 46], Schatten p -norm is proposed [47, 48, 49], which is defined as the ℓ_p -norm ($0 < p < 1$) of the

singular values. Compared with traditional nuclear norm, Schatten p -norm not
55 only achieves a more accurate recovery result of the signal, but also requires
only a *weaker restricted isometry property* based on theory [48]. Nonetheless,
similar to the standard nuclear norm, most of the Schatten p -norm based mod-
els treat all singular values equally, which may be infeasible in executing many
practical problems, such as image inverse problems [50]. To further improve
60 the flexibility of NNM, Gu *et al.* [4] proposed the weighted nuclear norm min-
imization (WNNM) model. Actually, the weighted nuclear norm is essentially
the reweighted ℓ_1 -norm of the singular values. Compared with NNM, WNNM
assigns different weights to different singular values such that the matrix rank
approximation become more reasonable.

65 Inspired by the success of ℓ_p ($0 < p < 1$) [44, 45, 46] and the reweighted ℓ_1
sparse optimization [51], to obtain the rank approximation more accurately, we
propose a novel model for image restoration (IR) via the non-convex weighted ℓ_p
($0 < p < 1$) nuclear norm minimization (NCW-NNM), which is expected to be
more accurate than traditional nuclear norm. Moreover, to solve the associated
70 non-convex minimization problem, we develop an efficient alternative direction
multiplier method (ADMM). Experimental results on three typical IR tasks,
including image deblurring, image inpainting and image compressive sensing
(CS) recovery, show that the proposed method outperforms many current state-
of-the-art methods both quantitatively and qualitatively.

75 The remainder of this paper is organized as follows. Section 2 introduces the
proposed non-convex weighted ℓ_p nuclear norm prior model for image restora-
tion. Section 3 presents the implementation details of the proposed non-convex
model under the ADMM optimization framework. Section 4 reports the exper-
imental results. Finally, Section 5 concludes this paper.

80 **2. Non-convex Weighted ℓ_p Nuclear Norm Prior Model for Image Restoration**

Generally speaking, the low rank property of the data matrix formed by nonlocal similar patches in image restoration (IR), is usually characterized by the nuclear norm. However, nuclear norm based convex surrogate of the rank function usually over-shrinks the rank components and makes different components equally, and thus may produce a result far from the optimum. To boost the accuracy of the rank approximation in IR, we propose an efficient IR method via the non-convex weighted ℓ_p nuclear norm minimization (NCW-NNM).

In this section, we will elaborate the non-convex weighted ℓ_p nuclear norm prior model for IR. Specifically, the basic idea is that data matrix composed of nonlocal similar patches in a natural image is of low rank. The well-known nonlocal self-similarity (NSS) [1, 4, 6, 7, 22, 26, 27, 28, 29, 30], which depicts the repetitiveness of textures and structures reflected by a natural image within nonlocal regions, implies that many similar patches can be found for any exemplar patch. More specifically, image \mathbf{X} with size N is divided into n overlapped patches \mathbf{x}_i of size $\sqrt{d} \times \sqrt{d}$, $i = 1, 2, \dots, n$. Then for each exemplar patch \mathbf{x}_i , its most similar m patches are selected from an $L \times L$ sized searching window to form a set \mathbf{S}_i . After this, all the patches in \mathbf{S}_i are stacked into a data matrix $\mathbf{X}_i \in \mathbb{R}^{d \times m}$, which contains every element of \mathbf{S}_i as its column, i.e., $\mathbf{X}_i = \{\mathbf{x}_{i,1}, \mathbf{x}_{i,2}, \dots, \mathbf{x}_{i,m}\}$, where $\mathbf{x}_{i,m}$ denotes the m -th similar patch (column vector form) of the i -th group. Since all the patches have the similar structures in each data matrix, thus, the constructed data matrix \mathbf{X}_i has a low-rank property. Therefore, by incorporating the low-rank prior into Eq. (2), IR is turned into solving the following minimization problem,

$$\hat{\mathbf{X}} = \arg \min_{\mathbf{X}} \frac{1}{2} \|\mathbf{Y} - \mathbf{H}\mathbf{X}\|_2^2 + \lambda \sum_{i=1}^n \mathbf{Rank}(\mathbf{X}_i) \quad (3)$$

In general, the rank minimization is an NP-hard problem. Most of methods resort to using the nuclear norm minimization (NNM) [43, 31, 33] as a convex relaxation of the non-convex rank minimization. However, since the singular

values have clear meanings and should be treated differently, NNM regularizes each of them equally, which cannot achieve the approximation of the matrix rank accurately. Inspired by the success of ℓ_p ($0 < p < 1$) [44, 45, 46] and the reweighted ℓ_1 sparse optimization [51], we introduce a more flexible non-convex weighted ℓ_p nuclear norm prior model. To be concrete, the weighted ℓ_p nuclear norm of a matrix $\mathbf{X}_i \in \mathfrak{R}^{d \times m}$, which is defined as

$$\mathbf{F}(\mathbf{X}_i) = \left(\sum_{j=1}^{\min\{d,m\}} w_{i,j} \sigma_{i,j}(\mathbf{X}_i)^p \right)^{\frac{1}{p}} \quad (4)$$

where $0 < p < 1$, and $\sigma_{i,j}(\mathbf{X}_i)$ is the j -th singular value of a matrix $\mathbf{X}_i \in \mathfrak{R}^{d \times m}$. $w_{i,j} \geq 0$ is a non-negative weight assigned to $\sigma_{i,j}(\mathbf{X}_i)$. Then the weighted ℓ_p nuclear norm of \mathbf{X}_i with power p is

$$\mathbf{F}(\mathbf{X}_i) = \sum_{j=1}^{\min\{d,m\}} w_{i,j} \sigma_{i,j}(\mathbf{X}_i)^p = \text{Tr}(\mathbf{W}_i \mathbf{\Sigma}_i^p) \quad (5)$$

where \mathbf{W}_i and $\mathbf{\Sigma}_i$ are diagonal matrices whose diagonal entries are composed of all $w_{i,j}$ and $\sigma_{i,j}(\mathbf{X}_i)$, respectively.

Therefore, considering all the data matrices $\{\mathbf{X}_i\}$, the proposed non-convex low rank prior model for IR is formulated as

$$\hat{\mathbf{X}} = \arg \min_{\mathbf{X}} \frac{1}{2} \|\mathbf{Y} - \mathbf{H}\mathbf{X}\|_2^2 + \lambda \sum_{i=1}^n \mathbf{F}(\mathbf{X}_i) \quad (6)$$

Obviously, it can be seen that the proposed non-convex low-rank prior model is able to employ the structured sparsity of nonlocal similar patches and the non-convexity of rank minimization simultaneously, which is expected to obtain better rank approximation results than many existing methods.

95 **3. Non-convex Weighted ℓ_p Nuclear Norm based ADMM Framework for Image Restoration**

In this section, the proposed scheme is used to solve the IR tasks, including image deblurring, image inpainting and image compressive sensing (CS) recovery. To be concrete, it can be seen that solving the objective function of Eq. (6) is very difficult, since it is a large scale non-convex optimization problem. To

make the proposed scheme tractable and robust, in this paper, we adopt the alternating direction method of multipliers (ADMM) [52] to solve Eq. (6).

The ADMM algorithm is a powerful tool for various large scale optimization problems and its basic idea is to turn the unconstrained minimization problem into a constrained one based on variable splitting. Numerical simulations have shown that it can converge by only using a small memory footprint, which makes it very attractive for numerous large-scale optimization problems [44, 53, 54]. We will briefly introduce the ADMM algorithm by considering a constrained optimization,

$$\min_{\mathbf{u} \in \mathfrak{R}^N, \mathbf{z} \in \mathfrak{R}^M} f(\mathbf{u}) + g(\mathbf{z}), \quad s.t. \quad \mathbf{u} = \mathbf{z} \quad (7)$$

where $\mathbf{z} \in \mathfrak{R}^{M \times N}$ and $f : \mathfrak{R}^N \rightarrow \mathfrak{R}$, $g : \mathfrak{R}^M \rightarrow \mathfrak{R}$. The complete description of the ADMM is shown in Algorithm 1.

Algorithm 1: ADMM Method.

1. **Initialization** k , choose $\rho > 0$, \mathbf{u} , \mathbf{z} , and \mathbf{c} .
 2. **Repeat**
 3. $\mathbf{u}^{k+1} = \arg \min_{\mathbf{u}} f(\mathbf{u}) + \frac{\rho}{2} \|\mathbf{u} - \mathbf{z}^k - \mathbf{c}^k\|_2^2$;
 4. $\mathbf{z}^{k+1} = \arg \min_{\mathbf{z}} g(\mathbf{z}) + \frac{\rho}{2} \|\mathbf{u}^{k+1} - \mathbf{z} - \mathbf{c}^k\|_2^2$;
 5. $\mathbf{c}^{k+1} = \mathbf{c}^k - (\mathbf{u}^{k+1} - \mathbf{z}^{k+1})$;
 6. $k \leftarrow k + 1$;
 7. **Until** stopping criterion is satisfied.
-

¹⁰⁵ Now, by introducing an auxiliary variable \mathbf{Z} with the constraint $\mathbf{X} = \mathbf{Z}$, Eq. (6) can be rewritten as

$$\mathbf{X}^{k+1} = \min_{\mathbf{X}} \frac{1}{2} \|\mathbf{Y} - \mathbf{H}\mathbf{X}\|_2^2 + \frac{\rho}{2} \|\mathbf{X} - \mathbf{Z}^k - \mathbf{C}^k\|_2^2 \quad (8)$$

$$\mathbf{Z}^{k+1} = \min_{\mathbf{Z}} \frac{\rho}{2} \|\mathbf{X}^{k+1} - \mathbf{Z} - \mathbf{C}^k\|_2^2 + \lambda \sum_{i=1}^n \mathbf{F}(\mathbf{Z}_i) \quad (9)$$

and

$$\mathbf{C}^{k+1} = \mathbf{C}^k - (\mathbf{X}^{k+1} - \mathbf{Z}^{k+1}) \quad (10)$$

It can be seen that the minimization for Eq. (6) involves splitting two minimization sub-problems, i.e., \mathbf{X} and \mathbf{Z} sub-problems. Next, we will introduce that there is an efficient solution to each sub-problem. To avoid confusion, the
 110 subscribe k may be omitted for conciseness.

3.1. \mathbf{X} sub-problem

Given \mathbf{Z} , the \mathbf{X} sub-problem denoted by Eq. (8) becomes

$$\min_{\mathbf{X}} \mathbf{L}_1(\mathbf{X}) = \min_{\mathbf{X}} \frac{1}{2} \|\mathbf{Y} - \mathbf{H}\mathbf{X}\|_2^2 + \frac{\rho}{2} \|\mathbf{X} - \mathbf{Z} - \mathbf{C}\|_2^2 \quad (11)$$

Clearly, Eq. (11) has a closed-form solution and its solution can be expressed as

$$\hat{\mathbf{X}} = (\mathbf{H}^T \mathbf{H} + \rho \mathbf{I})^{-1} (\mathbf{H}^T \mathbf{Y} + \rho(\mathbf{Z} + \mathbf{C})) \quad (12)$$

where \mathbf{I} represents the identity matrix.

Due to the specific structure of \mathbf{H} in image deblurring and image inpainting, Eq. (11) can be computed without matrix inversion efficiently (more details can
 115 be seen in [55]).

However, \mathbf{H} is a random projection matrix without a special structure in image CS recovery, computing the inverse by Eq. (11) at each iteration is too costly to implement numerically. Thus, to avoid computing the matrix inversion, an iterative algorithm is highly desired for solving Eq. (11). In this work, we adopt the gradient descent method [56] with an optimal step to solve Eq. (11), i.e.,

$$\hat{\mathbf{X}} = \mathbf{X} - \mu \mathbf{q} \quad (13)$$

where \mathbf{q} is the gradient direction of the objective function $\mathbf{L}_1(\mathbf{X})$, and μ is the optimal step.

Therefore, in image CS recovery, it only requires an iterative calculation of the following equation to solve the \mathbf{X} sub-problem,

$$\hat{\mathbf{X}} = \mathbf{X} - \mu (\mathbf{H}^T \mathbf{H} \mathbf{X} - \mathbf{H}^T \mathbf{Y} + \rho(\mathbf{X} - \mathbf{Z} - \mathbf{C})) \quad (14)$$

where $\mathbf{H}^T \mathbf{H}$ and $\mathbf{H}^T \mathbf{Y}$ can be calculated in advance.

3.2. \mathbf{Z} sub-problem

Given \mathbf{X} , similarly, according to Eq. (9), the \mathbf{Z} sub-problem can be rewritten as

$$\min_{\mathbf{Z}} \mathbf{L}_2(\mathbf{Z}) = \min_{\mathbf{Z}} \frac{1}{2} \|\mathbf{Z} - \mathbf{R}\|_2^2 + \frac{\lambda}{\rho} \sum_{i=1}^n \mathbf{F}(\mathbf{Z}_i) \quad (15)$$

where $\mathbf{R} = \mathbf{X} - \mathbf{C}$. However, due to the high complex non-convex structure of $\mathbf{F}(\mathbf{Z}_i)$, it is difficult to solve Eq. (15). To obtain a tractable solution of Eq. (15), in this work, a general assumption is made, with which even a closed-form solution can be obtained. Specifically, \mathbf{R} can be regarded as some type of noisy observation of \mathbf{X} , and then the assumption is made that each element of $\mathbf{E} = \mathbf{Z} - \mathbf{R}$ follows an independent zero-mean distribution with variance δ^2 . The following conclusion can be proved with this assumption.

Theorem 1 Define $\mathbf{Z}, \mathbf{R} \in \mathfrak{R}^N$, $\mathbf{Z}_i, \mathbf{R}_i \in \mathfrak{R}^{d \times m}$, and $\mathbf{e}(j)$ as each element of error vector \mathbf{e} , where $\mathbf{e} = \mathbf{Z} - \mathbf{R}, j = 1, \dots, N$. Assume that $\mathbf{e}(j)$ follows an independent zero mean distribution with variance δ^2 , and thus for any $\varepsilon > 0$, we can represent the relationship between $\frac{1}{N} \|\mathbf{Z} - \mathbf{R}\|_2^2$ and $\frac{1}{K} \sum_{i=1}^n \|\mathbf{Z}_i - \mathbf{R}_i\|_2^2$ by the following property,

$$\lim_{\substack{N \rightarrow \infty \\ K \rightarrow \infty}} \mathbf{P}\left\{\left|\frac{1}{N} \|\mathbf{Z} - \mathbf{R}\|_2^2 - \frac{1}{K} \sum_{i=1}^n \|\mathbf{Z}_i - \mathbf{R}_i\|_F^2\right| < \varepsilon\right\} = 1 \quad (16)$$

where $\mathbf{P}(\bullet)$ represents the probability and $K = d \times m \times n$.

Proof: Owing to the assumption that $\mathbf{e}(j)$ follows an independent zero mean distribution with variance δ^2 , i.e., $\mathbf{E}[\mathbf{e}(j)] = 0$ and $\mathbf{Var}[\mathbf{e}(j)] = \delta^2$. Thus, it can be deduced that each $\mathbf{e}(j)^2$ is also independent, and the meaning of each $\mathbf{e}(j)^2$ is:

$$\mathbf{E}[\mathbf{e}(j)^2] = \mathbf{Var}[\mathbf{e}(j)] + [\mathbf{E}[\mathbf{e}(j)]]^2 = \delta^2, j = 1, 2, \dots, N \quad (17)$$

By invoking the *law of Large numbers* in probability theory, for any $\varepsilon > 0$, it leads to $\lim_{N \rightarrow \infty} \mathbf{P}\left\{\left|\frac{1}{N} \sum_{j=1}^N \mathbf{e}(j)^2 - \delta^2\right| < \frac{\varepsilon}{2}\right\} = 1$, i.e.,

$$\lim_{N \rightarrow \infty} \mathbf{P}\left\{\left|\frac{1}{N} \|\mathbf{Z} - \mathbf{R}\|_2^2 - \delta^2\right| < \frac{\varepsilon}{2}\right\} = 1 \quad (18)$$

Next, we denote the concatenation of all the groups \mathbf{Z}_i and \mathbf{R}_i , $i = 1, 2, \dots, n$, by \mathbf{Z} and \mathbf{R} , respectively. Meanwhile, we denote the error of each element

130 of $\mathbf{Z} - \mathbf{R}$ by $\mathbf{e}(k)$, $k = 1, 2, \dots, K$. We have also denote $\mathbf{e}(k)$ following an independent zero mean distribution with variance δ^2 .

Therefore, the same process applied to $\mathbf{e}(k)^2$ yields $\lim_{N \rightarrow \infty} \mathbf{P}\{|\frac{1}{N} \sum_{k=1}^N \mathbf{e}(k)^2 - \delta^2| < \frac{\varepsilon}{2}\} = 1$, i.e.,

$$\lim_{N \rightarrow \infty} \mathbf{P}\{|\frac{1}{N} \sum_{i=1}^n \|\mathbf{Z}_i - \mathbf{R}_i\|_2^2 - \delta^2| < \frac{\varepsilon}{2}\} = 1 \quad (19)$$

Obviously, considering Eqs. (18) and (19) together, we can prove Eq. (16).

Accordingly, based on *Theorem 1*, we have the following equation with a very large probability (restricted 1) at each iteration,

$$\frac{1}{N} \|\mathbf{Z} - \mathbf{R}\|_2^2 = \frac{1}{K} \sum_{i=1}^n \|\mathbf{Z}_i - \mathbf{R}_i\|_F^2 \quad (20)$$

Therefore, based on Eqs. (15) and (20), we have

$$\begin{aligned} & \min_{\mathbf{Z}} \frac{1}{2} \|\mathbf{Z} - \mathbf{R}\|_2^2 + \frac{\lambda}{\rho} \sum_{i=1}^n \mathbf{F}(\mathbf{Z}_i) \\ & = \min_{\mathbf{Z}_i} \sum_{i=1}^n \left(\frac{1}{2} \|\mathbf{Z}_i - \mathbf{R}_i\|_F^2 + \tau \mathbf{F}(\mathbf{Z}_i) \right) \end{aligned} \quad (21)$$

135 where $\mathbf{F}(\mathbf{Z}_i) = \sum_{j=1}^{\min\{d,m\}} w_{i,j} \sigma_{i,j}(\mathbf{Z}_i)^p$ and $0 < p < 1$. $\sigma_{i,j}(\mathbf{Z}_i)$ denotes the j -th singular value of the matrix \mathbf{Z}_i and $\tau = \lambda K / \rho N$. Obviously, one can observe that Eq. (21) can be efficiently minimized by solving n sub-problems for all the data matrices \mathbf{Z}_i . However, due to the fact that Eq. (21) is high non-convex, it seems to be very difficult to solve it. Nonetheless, to achieve an effective
140 solution of Eq. (21), we have the following Theorems.

Theorem 2 (von Neumann) For any two matrices $\mathbf{A}, \mathbf{B} \in \mathfrak{R}^{m \times n}$, $tr(\mathbf{A}^T \mathbf{B}) \leq tr(\sigma(\mathbf{A})^T \sigma(\mathbf{B}))$, where $\sigma(\mathbf{A})$ and $\sigma(\mathbf{B})$ are the ordered singular value matrices of \mathbf{A} and \mathbf{B} with the same order, respectively.

The proof can be seen in [71].

Theorem 3 Let $\mathbf{R}_i = \mathbf{U}_i \mathbf{\Delta}_i \mathbf{V}_i^T$ be the SVD of $\mathbf{R}_i \in \mathfrak{R}^{d \times m}$ and $\mathbf{\Delta}_i = diag(\gamma_{i,1}, \dots, \gamma_{i,j})$, $j = \min(d, m)$. The optimal solution \mathbf{Z}_i to problem Eq. (21) is $\mathbf{U}_i \mathbf{\Sigma}_i \mathbf{V}_i^T$, where $\mathbf{\Sigma}_i = diag(\sigma_{i,1}, \dots, \sigma_{i,j})$. Then the optimal solution of the j -th diagonal element $\sigma_{i,j}$ of the diagonal matrix $\mathbf{\Sigma}_i$ is solved by the following

problem,

$$\min_{\sigma_{i,j} \geq 0} \sum_{j=1}^j \left(\frac{1}{2} (\sigma_{i,j} - \gamma_{i,j})^2 + \tau w_{i,j} \sigma_{i,j}^p \right) \quad (22)$$

145 where $\sigma_{i,j}$ represents the j -th singular value of each data matrix \mathbf{Z}_i .

Proof: Suppose the SVD of \mathbf{Z}_i and \mathbf{R}_i are $\mathbf{Z}_i = \mathbf{P}_i \mathbf{\Sigma}_i \mathbf{Q}_i^T$ and $\mathbf{R}_i = \mathbf{U}_i \mathbf{\Delta}_i \mathbf{V}_i^T$, respectively, where $\mathbf{\Sigma}_i$ and $\mathbf{\Delta}_i$ are ordered singular value matrices with the same order. Then Eq. (21) can be rewritten as

$$\min_{\mathbf{Z}_i} \sum_{i=1}^n \left(\frac{1}{2} \|\mathbf{P}_i \mathbf{\Sigma}_i \mathbf{Q}_i^T - \mathbf{U}_i \mathbf{\Delta}_i \mathbf{V}_i^T\|_F^2 + \tau \text{tr}(\mathbf{W}_i \mathbf{\Sigma}_i^p) \right) \quad (23)$$

where $\mathbf{W}_i = \{w_{i,1}, w_{i,2}, \dots, w_{i,j}\}^T$ and $w_{i,j}$ is a non-negative weight assigned to $\mathbf{\Sigma}_i$.

Based on Theorem 2, we have

$$\begin{aligned} & \|\mathbf{P}_i \mathbf{\Sigma}_i \mathbf{Q}_i^T - \mathbf{U}_i \mathbf{\Delta}_i \mathbf{V}_i^T\|_F^2 \\ &= \text{tr}(\mathbf{\Sigma}_i \mathbf{\Sigma}_i^T) + \text{tr}(\mathbf{\Delta}_i \mathbf{\Delta}_i^T) - 2\text{tr}(\mathbf{Z}_i^T \mathbf{R}_i) \\ &\geq \text{tr}(\mathbf{\Sigma}_i \mathbf{\Sigma}_i^T) + \text{tr}(\mathbf{\Delta}_i \mathbf{\Delta}_i^T) - 2\text{tr}(\mathbf{\Sigma}_i^T \mathbf{\Delta}_i) \\ &= \|\mathbf{\Sigma}_i - \mathbf{\Delta}_i\|_F^2 \end{aligned} \quad (24)$$

where the equality holds only when $\mathbf{P}_i = \mathbf{U}_i$ and $\mathbf{Q}_i = \mathbf{V}_i$. Therefore, Eq. (21) is minimized when $\mathbf{P}_i = \mathbf{U}_i$ and $\mathbf{Q}_i = \mathbf{V}_i$, and the optimal solution of $\mathbf{\Sigma}_i$ is obtained by solving the following problem,

$$\begin{aligned} & \min_{\mathbf{\Sigma}_i \geq 0} \frac{1}{2} \|\mathbf{\Sigma}_i - \mathbf{\Delta}_i\|_F^2 + \text{tr}(\mathbf{W}_i \mathbf{\Sigma}_i^p) \\ &= \min_{\sigma_{i,j} \geq 0} \sum_{j=1}^j \left(\frac{1}{2} (\sigma_{i,j} - \gamma_{i,j})^2 + \tau w_{i,j} \sigma_{i,j}^p \right) \end{aligned} \quad (25)$$

Therefore, the minimization problem of Eq. (21) can be simplified by minimizing the problem of Eq. (22).

Therefore, based on Theorem 2, the problem of Eq. (21) is transformed into solving Eq. (22). To obtain the solution of Eq. (22) effectively, in this subsection, the generalized soft-thresholding (GST) algorithm [45] is used to solve Eq. (22). More specifically, given p , $\gamma_{i,j}$ and $w_{i,j}$, there exists a specific threshold,

$$\tau_p^{GST}(w_{i,j}) = (2w_{i,j}(1-p))^{\frac{1}{2-p}} + w_{i,j} p (2w_{i,j}(1-p))^{\frac{p-1}{2-p}} \quad (26)$$

Here if $\gamma_{i,j} < \tau_p^{GST}(w_{i,j})$, $\sigma_{i,j} = 0$ is the global minimum. Otherwise, the optimum will be obtained at non-zero point. According to [45], for any $\gamma_{i,j} \in (\tau_p^{GST}(w_{i,j}), +\infty)$, Eq. (22) has one unique minimum $\mathbf{T}_p^{GST}(\gamma_{i,j}; w_{i,j})$, which can be obtained by solving the following equation,

$$\mathbf{T}_p^{GST}(\gamma_{i,j}; w_{i,j}) - \gamma_{i,j} + w_{i,j}p (\mathbf{T}_p^{GST}(\gamma_{i,j}; w_{i,j}))^{p-1} = 0 \quad (27)$$

150 The complete description of the GST algorithm is exhibited in Algorithm 2. For more details about the GST algorithm, please refer to [45].

Algorithm 2: Generalized Soft-Thresholding (GST) [45].

Input: $\gamma_{i,j}, w_{i,j}, p, J$.

1. $\tau_p^{GST}(w_{i,j}) = (2w_{i,j}(1-p))^{\frac{1}{2-p}} + w_{i,j}p(2w_{i,j}(1-p))^{\frac{p-1}{2-p}}$;
2. **If** $|\gamma_{i,j}| \leq \tau_p^{GST}(w_{i,j})$
3. $\mathbf{T}_p^{GST}(\gamma_{i,j}; w_{i,j}) = 0$;
4. **else**
5. $t = 0, \sigma_{i,j}^{(t)} = |\gamma_{i,j}|$;
6. Iterate on $t = 0, 1, \dots, J$
7. $\sigma_{i,j}^{(t+1)} = |\gamma_{i,j}| - w_{i,j}p (\sigma_{i,j}^{(t)})^{p-1}$;
8. $t \leftarrow t + 1$;
9. $\mathbf{T}_p^{GST}(\gamma_{i,j}; w_{i,j}) = \text{sgn}(\gamma_{i,j})\sigma_{i,j}^t$;
10. **End**

Input:: $\mathbf{T}_p^{GST}(\gamma_{i,j}; w_{i,j})$.

Therefore, a closed-form solution of Eq. (22) can be computed as

$$\sigma_{i,j} = GST(\gamma_{i,j}, \tau w_{i,j}, p, J) \quad (28)$$

where J denotes the iteration number of the GST algorithm.

For each weight $w_{i,j}$, large singular values of a group \mathbf{R}_i transmit major edge and texture information. This implies that to reconstruct \mathbf{X}_i from its degraded one, we should shrink the larger singular values less, while shrinking smaller ones more. Therefore, we let

$$w_{i,j} = \frac{1}{|\gamma_{i,j}| + \epsilon} \quad (29)$$

where ϵ is a small constant.

The parameter λ that balances the fidelity term and the regularization term should be adaptively determined for better reconstruction performance. In this paper, inspired by [57], the regularization parameter λ of each group \mathbf{R}_i is set as:

$$\lambda = \frac{2\sqrt{2}\delta^2}{\theta_i + \varsigma} \quad (30)$$

where θ_i denotes the estimated variance of $\mathbf{\Delta}_i$, and ς is a small constant.

155 3.3. Summary of the Algorithm

The above two sub-problems \mathbf{X} , \mathbf{Z} have been solved. We can achieve an efficient solution by solving each sub-problem separately, which can guarantee the whole algorithm to be more efficient and effective. Based on the above analysis, the complete description of the proposed method for the IR via non-convex weighted ℓ_p nuclear norm prior model is exhibited in Table 1.

4. Experimental Results

In this section, we conduct a variety of experiments on three IR tasks, including image deblurring, image inpainting and image CS recovery, to evaluate the effectiveness of the proposed NCW-NNM method. To prove the advantage of the proposed NCW-NNM method, which can improve the accuracy of the matrix rank approximation. We compare it with traditional rank minimization method, i.e., nuclear norm minimization (NNM) method. All the experimental images are shown in Fig. 1. To evaluate the quality of the restored images, the PSNR and the recently proposed powerful perceptual quality metric FSIM [58] are calculated. All the experiments were implemented in Matlab 2012b on a PC with 3.50GHz CUP and 4GB RAM.

4.1. Image Deblurring

In image deblurring, two blur kernels, 9×9 uniform kernel and a Gaussian blur kernel (`fspecial('gaussian', 25, 1.6)`) are used. Blurred images are further

Table 1: The Proposed NCW-NNM model for Image Restoration.

Input: The observed image \mathbf{Y} , the degraded operator \mathbf{H} .

Initialization: k , \mathbf{C} , \mathbf{Z} , d , m , ρ , p , δ , ϵ , ς , L , K ;

Repeat

If \mathbf{H} is blur operator or mask operator

Update \mathbf{X}^{k+1} computing by Eq. (12);

Else \mathbf{H} is random projection operator

Update \mathbf{X}^{k+1} computing by Eq. (14);

End if

$\mathbf{R}^{k+1} = \mathbf{X}^{k+1} - \mathbf{C}^k$;

Generating the groups $\{\mathbf{R}_i\}$ by searching similar patches from \mathbf{R} ;

For Each group \mathbf{R}_i **do**

Singular value decomposition $[\mathbf{U}_i, \mathbf{\Delta}_i, \mathbf{V}_i] = SVD(\mathbf{R}_i)$;

Update the weight \mathbf{W}_i^{k+1} computing by Eq. (29)

Update λ^{k+1} computing by Eq. (30);

Calculate $\mathbf{\Sigma}_i$ by using Eq. (28);

Get the estimation $\mathbf{Z}_i^{k+1} = \mathbf{U}_i \mathbf{\Sigma}_i \mathbf{V}_i^T$;

End for

Update \mathbf{Z}^{k+1} by aggregating all groups \mathbf{Z}_i^{k+1} ;

Update \mathbf{C}^{k+1} by computing Eq. (10);

$k \leftarrow k + 1$;

End for

Until

maximum iteration number is reached.

Output:

The final restored image $\hat{\mathbf{X}}$.



Figure 1: All test images. Top: Barbara, boats, Butterfly, fingerprint, Flower, Leaves, House, Castle. Below: Zebra, Corn, starfish, Fence, Girl, Light, pentagon, Mickey.

175 corrupted by additive white Gaussian noise with $\delta = \sqrt{2}$. The parameters are set as follows. The size of each patch $\sqrt{d} \times \sqrt{d}$ is set to 8×8 . Similar patch numbers $m = 60$, $L = 25$, $\epsilon = 0.1$, $\varsigma = 0.3$, $J = 2$. (ρ, p) are set to $(0.02, 0.7)$ and $(0.06, 0.6)$ for Gaussian blur and Uniform blur, respectively.

We have compared the proposed NCW-NNM with five other competing
 180 methods including BM3D [59], NCSR [26], JSM [7], MSEPLL [60] and FPD [61]. The PSNR and FSIM results are shown in Table 2. The average gain of the proposed NCW-NNM over BM3D, NCSR, JSM, MSEPLL and FPD methods can be as much as 0.64dB, 0.16dB, 1.07dB, 0.79dB and 1.85dB, respectively. The visual comparisons of the deblurring methods are shown in Fig. 2 and Fig. 3.
 185 It can be seen that BM3D, NCSR, JSM, MSEPLL and FPD still generate some undesirable artifacts, while result in over-smooth phenomena. By contrast, the proposed NCW-NNM not only preserves the sharpness of edges, but also suppresses undesirable artifacts more efficiently.

In addition, the proposed NCW-NNM is compared with AKTV method [62],
 190 where AKTV method is well-known for working quite well in the case of large blur. Here, 19×19 uniform kernel with the corresponding BSNR=40 for image *Fence* is tested, where BSNR means Blurred Signal to Noise Ratio, and it is equivalent to $10 \cdot \log(\text{Blurred Signal variance}/\text{Noise variance})$. Smaller BSNR means larger noise variance. All the parameters are the same as specified in
 195 the case of 9×9 uniform kernel except for $\rho = 0.00002$. The visual quality

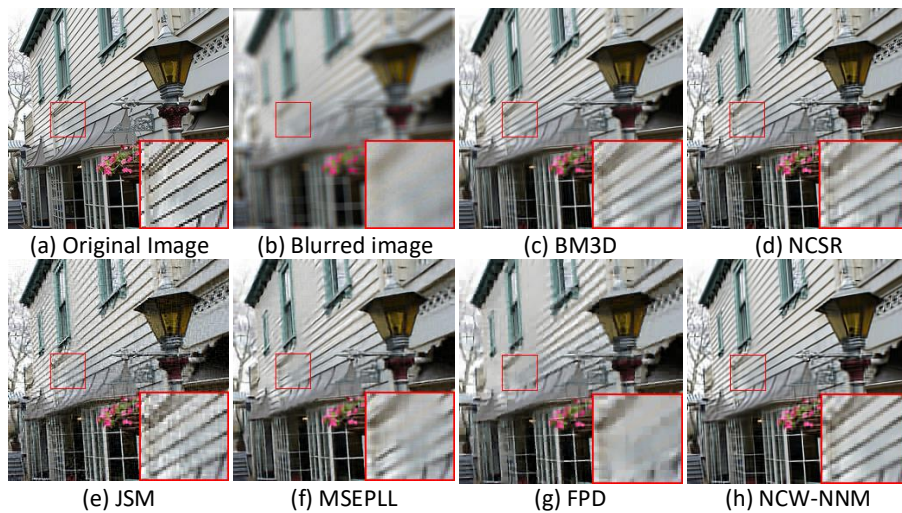


Figure 2: Visual comparison of *Light* by image deblurring with 9×9 Uniform Kernel, $\delta = \sqrt{2}$. (a) Original image; (b) Noisy and blurred image; (c) deblurred image by (c) BM3D [59] (PSNR = 21.65dB, FSIM= 0.8423); (d) NCSR [26] (PSNR = 22.10dB, FSIM = 0.8733); (e) JSM [7] (PSNR =21.84dB, FSIM = 0.8439); (f) MSEPLL [60] (PSNR = 21.27dB, FSIM = 0.8417); (g) FPD [61] (PSNR = 19.70dB, FSIM = 0.7725); (h) NCW-NNM (PSNR =**22.58dB**, FSIM =**0.8790**).

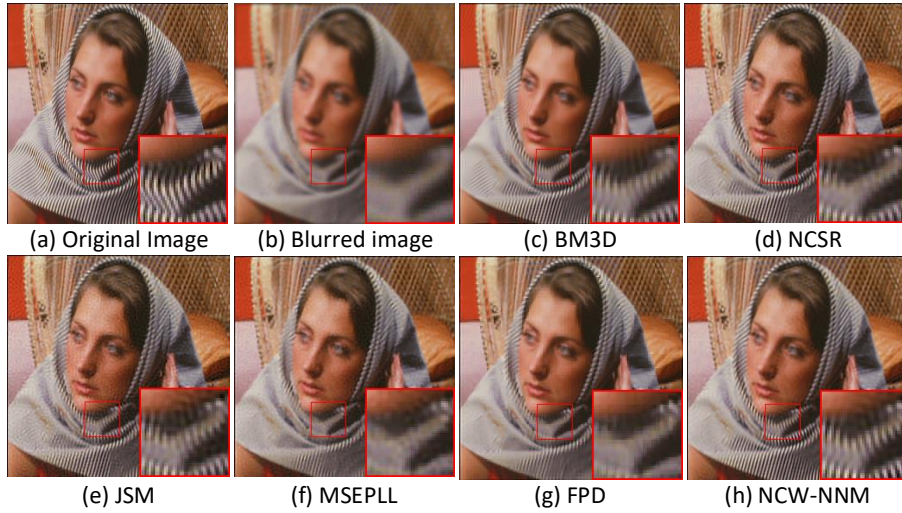


Figure 3: Visual comparison of *Barbara* by image deblurring with Gaussian blur: special('gaussian', 25, 1.6), $\delta = \sqrt{2}$. (a) Original image; (b) Noisy and blurred image; (c) deblurred image by (c) BM3D [59] (PSNR = 25.77dB, FSIM= 0.8802); (d) NCSR [26] (PSNR = 25.95dB, FSIM = 0.8853); (e) JSM [7] (PSNR = 25.89dB, FSIM = 0.8752); (f) MSEPLL [60] (PSNR = 24.82dB, FSIM = 0.8579); (g) FPD [61] (PSNR = 24.54dB, FSIM = 0.8622); (h) NCW-NNM (PSNR = **26.72dB**, FSIM = **0.9009**).

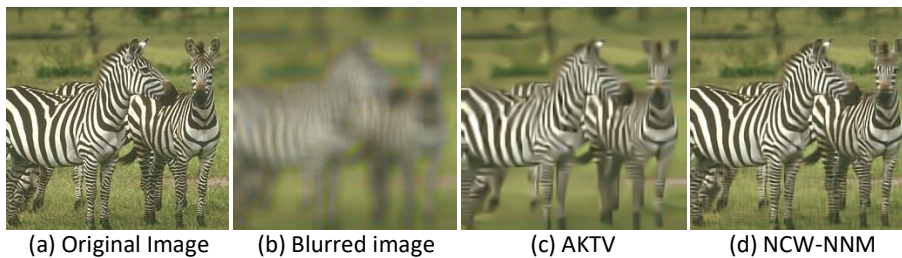


Figure 4: Deblurring performance comparison on the *Zebra* image. (a) Original image; (b) Noisy and blurred image (19×19 uniform blur, BSNR=40); deblurred image by (c) AKTV [62] (PSNR = 21.18dB, FSIM = 0.7394); (d) NCW-NNM (PSNR = **26.15dB**, FSIM = **0.9028**).

comparison is shown in Fig. 4. It can be seen that the proposed NCW-NNM produces much clear and preserves much more details than AKTV method.

Table 2: PSNR/FSIM Comparisons for Image Deblurring.

Gaussian Kernel: fspecial('gaussian', 25, 1.6), $\delta = \sqrt{2}$						
Method	<i>Light</i>	<i>Barbara</i>	<i>Fence</i>	<i>Flower</i>	<i>Zebra</i>	Average
BM3D [59]	21.75/0.8430	25.77/0.8802	27.31/0.8936	29.84/0.9100	24.64/0.8666	25.86/0.8787
NCSR [26]	22.28 /0.8667	25.95/0.8853	27.40/0.9087	30.21/0.9187	25.05/0.8868	26.18/0.8932
JSM [7]	22.24/0.8612	25.89/0.8752	27.08/0.9026	29.52/0.8878	24.66/0.8722	25.88/0.8798
MSEPLL [60]	21.93/0.8634	24.82/0.8579	27.12/0.8933	30.35/0.9234	24.75/0.8864	25.79/0.8849
FPD [61]	21.12/0.8319	24.54/0.8622	26.54/0.8886	30.46/0.9354	24.01/0.8716	25.33/0.8780
NNM	21.88/0.8496	25.90/0.8795	27.35/0.9074	29.94/0.9040	24.60/0.8721	25.93/0.8825
NCW-NNM	22.26/ 0.8683	26.72/0.9009	27.57/0.9136	30.27/0.9230	24.88/0.8805	26.34/0.8973
9×9 Uniform Kernel, $\delta = \sqrt{2}$						
Method	<i>Light</i>	<i>Barbara</i>	<i>Fence</i>	<i>Flower</i>	<i>Zebra</i>	Average
BM3D [59]	21.65/0.8423	26.89/0.8807	28.94/0.9045	28.54/0.8732	23.69/0.8330	25.94/0.8667
NCSR [26]	22.10/0.8733	27.12/0.9006	29.83/ 0.9302	29.28 /0.9001	24.63/0.8743	26.59/0.8957
JSM [7]	21.84/0.8439	25.72/0.8600	27.26/0.9036	27.15/0.8257	23.32/0.8274	25.06/0.8521
MSEPLL [60]	21.27/0.8417	26.24/0.8756	28.02/0.8935	29.07/0.8881	23.98/0.8566	25.72/0.8711
FPD [61]	19.70/0.7725	25.22/0.8519	25.25/0.8390	28.49/0.8799	21.62/0.7882	24.06/0.8263
NNM	21.82/0.8579	27.02/0.8945	29.76/0.9284	28.91/0.8875	23.84/0.8541	26.27/0.8845
NCW-NNM	22.58/0.8790	27.48/0.9092	29.98 /0.9300	29.27/ 0.9043	24.43/0.8682	26.75/0.8981

4.2. Image Inpainting

In this subsection, two interesting examples of image inpainting with different masks are conducted, i.e., image restoration from partial random samples and text inlayed sample. The parameters are set as follows. The size of each patch $\sqrt{d} \times \sqrt{d}$ is set to be 8×8 and 10×10 for partial random samples and text inlayed, respectively. Similar patch numbers $m = 60$, $L = 25$, $\epsilon = 0.1$, $\varsigma = 0.3$, $J = 2$. (ρ, p) are set to $(0.0003, 0.45)$, $(0.0003, 0.45)$, $(0.03, 0.95)$, $(0.04, 0.95)$ and $(0.06, 0.95)$ when 80%, 70%, 60%, 50% pixels missing and text inlayed, respectively.

We compare the proposed NCW-NNM with five other competing methods: SALSA [63], BPFA [10], IPPO [64], JSM [7] and Aloha [9]. Table 3 lists the

PSNR and FSIM comparison results. In terms of PSNR, the proposed NCW-
 210 NNM achieves 3.52dB, 2.26dB, 1.10dB, 1.27dB and 1.98dB improvement on
 average over the SALSA, BPFA, IPPO, JSM and Aloha, respectively. The
 visual comparisons of the image inpainting methods are shown in Fig. 5 and
 Fig. 6. It can be seen that SALSA, BPFA, IPPO, JSM and Aloha still generate
 some undesirable ringing effects and some details are lost. In contract, the
 215 proposed NCW-NNM not only preserves sharper edges and finer details, but
 also significantly eliminates the ringing effects.



Figure 5: Visual comparison of *Girl* by image inpainting with 80% pixels missing. (a) Original image; (b) Degraded image with 80% missing sample; Restoration by (c) SALSA [63] (PSNR = 23.80dB, FSIM = 0.8517); (d) BPFA [10] (PSNR = 24.80dB, FSIM = 0.8765); (e) IPPO [64] (PSNR = 25.31dB, FSIM = 0.8914); (f) JSM [7] (PSNR = 25.18dB, FSIM = 0.8871); (g) Aloha [9] (PSNR = 25.17dB, FSIM = 0.8832); (h) NCW-NNM (PSNR = **25.78dB**, FSIM = **0.9065**).

4.3. Image Compressive Sensing Recovery

In this subsection, we show the experimental results of the proposed NCW-
 NNM based image CS recovery. We generate the CS measurements at the block
 220 level by exploiting Gaussian random projection matrix to test images, i.e., the

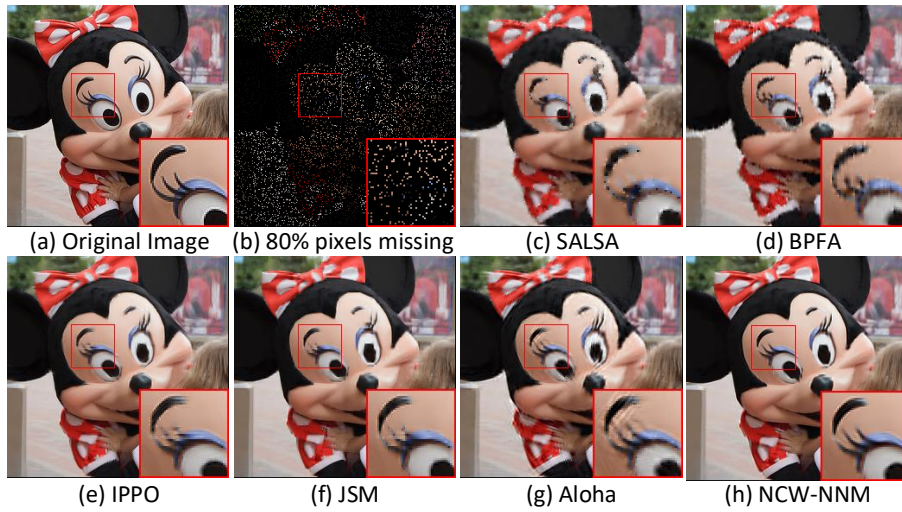


Figure 6: Visual comparison of *Mickey* by image inpainting with 80% pixels missing. (a) Original image; (b) Degraded image with 80% missing sample; Restoration by (c) SALSA [63] (PSNR = 24.46dB, FSIM = 0.8693); (d) BPFA [10] (PSNR = 24.53dB, FSIM = 0.8696); (e) IPPO [64] (PSNR = 26.33dB, FSIM = 0.9099); (f) JSM [7] (PSNR = 26.09dB, FSIM = 0.9060); (g) Aloha [9] (PSNR = 25.33dB, FSIM = 0.8770); (h) NCW-NNM (PSNR = **26.92dB**, FSIM = **0.9214**).

Table 3: PSNR/FSIM Comparisons for Image Inpainting.

80% pixels missing						
Method	<i>Mickey</i>	<i>Butterfly</i>	<i>Castle</i>	<i>Corn</i>	<i>Girl</i>	Average
SALSA [63]	24.46/0.8693	22.85/0.8451	22.85/0.8319	24.28/0.8803	23.80/0.8517	23.65/0.8557
BPFA [10]	24.53/0.8696	24.04/0.8532	23.94/0.8639	25.54/0.9010	24.80/0.8765	24.57/0.8729
IPPO [64]	26.33/0.9099	25.13/0.9078	24.50/0.8818	25.14/0.9020	25.31/0.8914	25.28/0.8986
JSM [7]	26.09/0.9060	25.57/0.9125	24.59/0.8830	25.58/0.9089	25.18/0.8871	25.40/0.8995
Aloha [9]	25.33/0.8770	24.88/0.8586	23.88/0.8728	25.60/0.8963	25.16/0.8832	24.97/0.8775
NNM	25.97/0.9011	25.61/0.9125	24.35/0.8689	25.68/0.9076	25.18/0.8824	25.36/0.8945
NCW-NNM	26.92/0.9214	26.52/0.9271	24.84/0.8953	26.87/0.9287	25.78/0.9065	26.19/0.9158
70% pixels missing						
Method	<i>Mickey</i>	<i>Butterfly</i>	<i>Castle</i>	<i>Corn</i>	<i>Girl</i>	Average
SALSA [63]	25.98/0.9033	25.06/0.8909	24.22/0.8761	26.11/0.9193	25.48/0.8932	25.37/0.8965
BPFA [10]	26.16/0.9058	26.68/0.9077	25.66/0.9048	27.82/0.9366	26.86/0.9157	26.64/0.9141
IPPO [64]	28.59/0.9406	27.69/0.9401	26.11/0.9162	27.77/0.9409	27.43/0.9316	27.52/0.9339
JSM [7]	28.25/0.9356	27.97/0.9430	26.64/0.9217	27.67/0.9412	27.20/0.9275	27.55/0.9338
Aloha [9]	27.11/0.9107	27.29/0.8996	25.77/0.9101	27.95/0.9314	27.08/0.9211	27.04/0.9146
NNM	27.86/0.9311	27.86/0.9414	26.15/0.9108	27.63/0.9390	26.92/0.9209	27.28/0.9286
NCW-NNM	29.29/0.9474	29.28/0.9532	26.87/0.9295	29.29/0.9562	28.09/0.9419	28.56/0.9456
60% pixels missing						
Method	<i>Mickey</i>	<i>Butterfly</i>	<i>Castle</i>	<i>Corn</i>	<i>Girl</i>	Average
SALSA [63]	27.41/0.9262	26.79/0.9199	25.73/0.9093	27.75/0.9438	27.02/0.9244	26.94/0.9247
BPFA [10]	23.65/0.9186	28.88/0.9394	27.28/0.9313	30.07/0.9590	28.75/0.9417	27.73/0.9380
IPPO [64]	30.77/0.9592	29.85/0.9600	27.81/0.9396	29.75/0.9610	29.32/0.9528	29.50/0.9545
JSM [7]	29.85/0.9536	29.83/0.9600	28.09/0.9426	29.45/0.9610	29.01/0.9501	29.25/0.9535
Aloha [9]	28.59/0.9342	29.16/0.9242	27.16/0.9298	29.83/0.9526	28.91/0.9434	28.73/0.9368
NNM	29.61/0.9508	29.82/0.9595	27.61/0.9359	29.33/0.9587	28.71/0.9462	29.02/0.9500
NCW-NNM	31.46/0.9643	31.54/0.9690	28.44/0.9484	31.52/0.9724	30.23/0.9624	30.64/0.9633
50% pixels missing						
Method	<i>Mickey</i>	<i>Butterfly</i>	<i>Castle</i>	<i>Corn</i>	<i>Girl</i>	Average
SALSA [63]	28.98/0.9458	28.52/0.9432	27.01/0.9314	29.39/0.9600	28.60/0.9455	28.50/0.9452
BPFA [10]	29.43/0.9501	30.98/0.9595	28.83/0.9488	32.10/0.9725	30.58/0.9597	30.38/0.9581
IPPO [64]	32.74/0.9719	31.69/0.9724	29.57/0.9576	31.76/0.9745	31.05/0.9672	31.36/0.9687
JSM [7]	31.96/0.9685	31.47/0.9720	29.48/0.9583	31.33/0.9743	30.68/0.9665	30.98/0.9679
Aloha [9]	30.33/0.9515	30.78/0.9414	28.71/0.9485	31.89/0.9679	30.60/0.9608	30.46/0.9540
NNM	31.62/0.9666	31.46/0.9715	29.17/0.9540	31.23/0.9731	30.40/0.9641	30.77/0.9659
NCW-NNM	34.01/0.9769	33.26/0.9785	30.15/0.9634	33.80/0.9828	32.13/0.9749	32.67/0.9753
Inlay text						
Method	<i>Mickey</i>	<i>Butterfly</i>	<i>Castle</i>	<i>Corn</i>	<i>Girl</i>	Average
SALSA [63]	30.67/0.9670	29.81/0.9617	28.75/0.9556	30.96/0.9736	30.27/0.9630	30.09/0.9642
BPFA [10]	31.71/0.9719	31.71/0.9683	30.94/0.9671	32.16/0.9782	31.28/0.9691	31.56/0.9710
IPPO [64]	34.04/0.9838	33.98/0.9840	31.91/0.9762	32.48/0.9815	32.65/0.9795	33.01/0.9810
JSM [7]	32.99/0.9811	33.19/0.9831	32.48/0.9769	32.26/0.9815	32.21/0.9772	32.62/0.9799
Aloha [9]	30.49/0.9641	31.58/0.9569	30.34/0.9672	32.04/0.9752	30.84/0.9693	31.06/0.9665
NNM	32.65/0.9794	33.00/0.9805	31.49/0.9727	32.15/0.9802	32.07/0.9753	32.27/0.9776
NCW-NNM	35.31/0.9869	34.89/0.9861	33.17/0.9809	33.98/0.9870	33.20/0.9818	34.11/0.9845

block-based CS recovery with block size of 32×32 . The parameters are set as follows. The size of each patch $\sqrt{d} \times \sqrt{d}$ is set to be 7×7 . The searching matched patches $m = 60$ and $L = 20$. We assign $\epsilon = 0.1$ and $\zeta = 0.4$. (p, ρ) are set to $(0.65, 0.0001)$, $(0.5, 0.0005)$, $(0.95, 0.005)$ and $(0.95, 0.005)$ when $0.1N$, $0.2N$, $0.3N$ and $0.4N$ measurements, respectively.

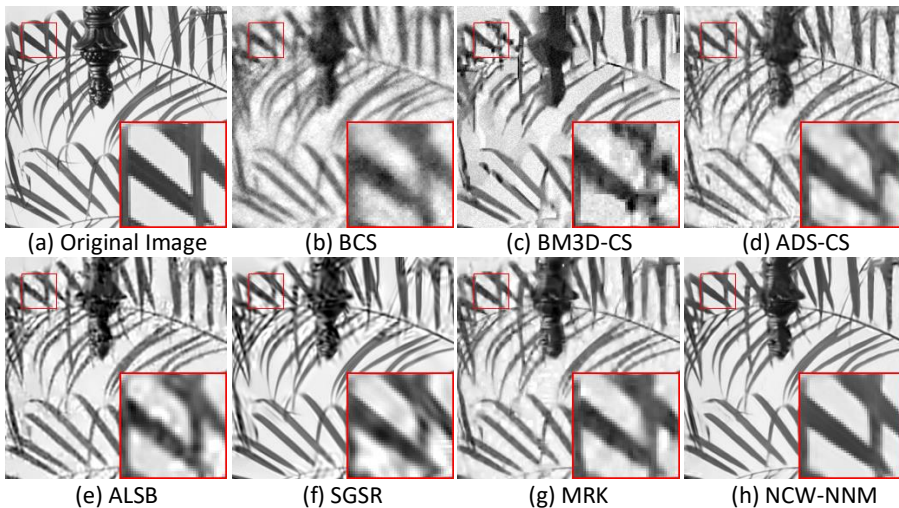


Figure 7: Visual comparison of *Leaves* by image CS recovery with $0.1N$ measurements. (a) Original image; (b) BCS [65] (PSNR = 18.55dB, FSIM = 0.5797); (c) BM3D-CS [66] (PSNR = 18.93dB, FSIM = 0.7259); (d) ADS-CS [15] (PSNR = 21.24dB, FSIM = 0.7671); (e) ALSB [23] (PSNR = 21.61dB, FSIM = 0.8010); (f) SGSR [67] (PSNR = 22.22dB, FSIM = 0.8356); (g) MRK [68] (PSNR = 22.05dB, FSIM = 0.8118); (h) NCW-NNM (PSNR = **22.05dB**, FSIM = **0.8118**).

225

To verify the performance of the proposed NCW-NNM, we have compared it with some competitive CS recovery methods including BCS [65], BM3D-CS [66], ADS-CS [15], ALSB [23], SGSR [67] and MRK [68] methods. The PSNR and FSIM results of 6 gray images are shown in Table 4. One can observe that the proposed NCW-NNM almost outperforms other competing methods on all test images over different numbers of CS measurements. The average gain of NCW-NNM over BCS, BM3D-CS, ADS-CS, ALSB, SGSR and MRK can be as

230

much as 6.48dB, 2.94dB, 1.28dB, 1.77dB, 1.76dB and 1.62dB, respectively. The visual comparison results of the recovered images are presented in Fig. 7 and Fig. 8. It can be seen that BCS method generates the worst perceptual result. The BM3D-CS, ADS-CS, ALSB, SGSR and MRK methods can obtain much better visual quality than BCS method, but still suffer from some undesirable artifacts or over-smooth phenomena, such as ring effects and some fine image details are lost. By contrast, the proposed NCW-NNM not only removes most of the visual artifacts, but also preserves large-scale sharp edges and small-scale fine image details more effective than other competing methods.

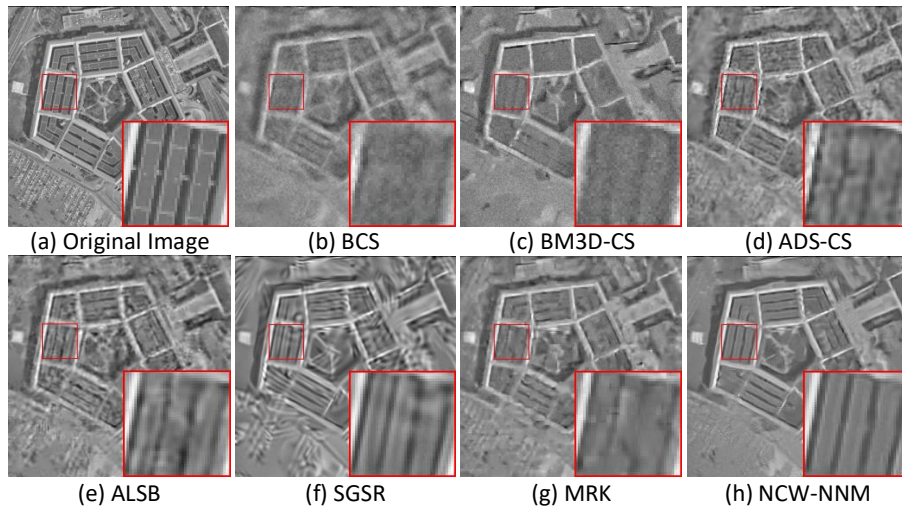


Figure 8: Visual comparison of *pentagon* by image CS recovery with $0.1N$ measurements. (a) Original image; (b) BCS [65] (PSNR = 22.14dB, FSIM = 0.5068); (c) BM3D-CS [66] (PSNR = 21.87dB, FSIM = 0.7443); (d) ADS-CS [15] (PSNR = 23.37dB, FSIM = 0.7999); (e) ALSB [23] (PSNR = 23.16dB, FSIM = 0.8059); (f) SGSR [67] (PSNR = 23.05dB, FSIM = 0.8060); (g) MRK [68] (PSNR = 23.70dB, FSIM = 0.7890); (h) NCW-NNM (PSNR = **24.26dB**, FSIM = **0.8064**).

4.4. Effect of the number of the best matched patches

In this subsection, we have discussed how to select the best matching patch numbers m for the performance of the proposed NCW-NNM method. Specifici-

Table 4: PSNR/FSIM Comparisons for Image CS Recovery.

Substrate = 0.1N							
Method	<i>boats</i>	<i>House</i>	<i>fingerprint</i>	<i>Leaves</i>	<i>pentagon</i>	<i>starfish</i>	Average
BCS [65]	24.54/0.6715	26.99/0.7681	17.10/0.3434	18.55/0.5797	22.14/0.5068	22.97/0.6687	22.05/0.5897
BM3D-CS [66]	25.40/0.8308	32.50/0.9146	16.02/0.6684	18.93/0.7259	21.87/0.7443	20.72/0.7591	22.57/0.7739
ADS-CS [15]	28.30/0.8886	33.39/0.9057	18.91/0.7714	21.24/0.7671	23.37/0.7999	25.50/0.8579	25.12/0.8318
ALSB [23]	28.09/0.8894	32.17/0.9107	20.68/0.8665	21.61/0.8010	23.16/0.8059	23.61/0.8305	24.89/0.8507
SGSR [67]	27.71/0.8915	32.77/0.9187	20.37/0.8671	22.22/0.8356	23.05/0.8060	22.91/0.8175	24.84/0.8560
MRK [68]	28.32/0.8906	32.43/0.9132	17.66/0.6774	22.05/0.8118	23.70/0.7890	25.27/0.8580	24.90/0.8233
NNM	27.91/0.8925	32.89/0.9260	21.33/0.8558	22.85/0.8880	24.02/0.7961	24.21/0.8484	25.70/0.8678
NCW-NNM	28.64/0.9019	33.52/0.9279	21.57/0.8684	25.77/0.9124	24.26/0.8064	25.49/0.8755	26.54/0.8821
Substrate = 0.2N							
Method	<i>boats</i>	<i>House</i>	<i>fingerprint</i>	<i>Leaves</i>	<i>pentagon</i>	<i>starfish</i>	Average
BCS [65]	27.05/0.8654	30.54/0.9011	18.50/0.7355	21.12/0.7531	23.97/0.8087	25.29/0.8624	24.41/0.8211
BM3D-CS [66]	31.01/0.9314	35.04/0.9498	19.38/0.8184	28.14/0.9232	25.49/0.8558	27.50/0.8964	27.76/0.8958
ADS-CS [15]	33.15/0.9508	35.76/0.9423	22.70/0.8976	27.88/0.9015	26.31/0.8801	30.22/0.9262	29.34/0.9164
ALSB [23]	32.96/0.9514	36.07/0.9563	23.69/0.9226	27.15/0.9089	26.19/0.8817	27.30/0.8984	28.89/0.9199
SGSR [67]	32.41/0.9466	35.81/0.9503	23.20/0.9186	28.74/0.9373	26.55/0.8947	27.13/0.8986	28.97/0.9243
MRK [68]	32.38/0.9476	36.36/0.9586	20.54/0.8397	27.75/0.9169	27.11/0.8888	29.18/0.9239	28.89/0.9126
NNM	31.68/0.9422	36.01/0.9580	23.57/0.9110	27.72/0.9373	26.60/0.8806	27.37/0.9092	28.83/0.9230
NCW-NNM	33.77/0.9576	36.92/0.9616	24.20/0.9287	31.46/0.9615	27.59/0.9072	29.99/0.9398	30.65/0.9427
Substrate = 0.3N							
Method	<i>boats</i>	<i>House</i>	<i>fingerprint</i>	<i>Leaves</i>	<i>pentagon</i>	<i>starfish</i>	Average
BCS [65]	28.91/0.8997	32.85/0.9299	19.96/0.8149	23.16/0.8018	25.54/0.8595	27.20/0.8968	26.27/0.8671
BM3D-CS [66]	34.04/0.9630	36.84/0.9689	23.02/0.9111	32.52/0.9602	28.20/0.9154	31.48/0.9444	31.02/0.9438
ADS-CS [15]	36.35/0.9728	38.21/0.9667	25.33/0.9408	32.55/0.9550	28.52/0.9217	32.90/0.9540	32.31/0.9518
ALSB [23]	36.42/0.9746	38.34/0.9732	25.84/0.9475	31.08/0.9511	28.22/0.9210	30.35/0.9408	31.71/0.9513
SGSR [67]	35.21/0.9683	37.37/0.9648	25.49/0.9455	32.98/0.9676	28.66/0.9318	30.78/0.9446	31.75/0.9538
MRK [68]	34.97/0.9687	38.35/0.9727	24.21/0.9225	32.37/0.9598	29.50/0.9337	32.53/0.9589	31.99/0.9527
NNM	34.18/0.9641	37.94/0.9721	25.27/0.9379	30.99/0.9619	28.41/0.9194	30.07/0.9422	31.14/0.9496
NCW-NNM	37.11/0.9772	39.23/0.9766	26.48/0.9544	35.17/0.9798	29.74/0.9429	33.38/0.9654	33.52/0.9661
Substrate = 0.4N							
Method	<i>boats</i>	<i>House</i>	<i>fingerprint</i>	<i>Leaves</i>	<i>pentagon</i>	<i>starfish</i>	Average
BCS [65]	30.56/0.9248	34.65/0.9490	21.67/0.8747	25.07/0.8422	27.00/0.8950	28.94/0.9217	27.98/0.9012
BM3D-CS [66]	36.71/0.9805	38.08/0.9781	25.47/0.9451	36.01/0.9816	30.53/0.9483	34.27/0.9675	33.51/0.9669
ADS-CS [15]	38.79/0.9835	40.30/0.9803	27.32/0.9608	35.94/0.9763	30.64/0.9488	35.36/0.9721	34.73/0.9703
ALSB [23]	38.92/0.9840	40.25/0.9824	27.70/0.9638	34.57/0.9738	29.84/0.9422	32.98/0.9619	34.04/0.9680
SGSR [67]	37.41/0.9794	38.99/0.9759	27.64/0.9645	35.83/0.9799	30.66/0.9548	33.66/0.9661	34.03/0.9701
MRK [68]	37.20/0.9802	40.04/0.9819	26.83/0.9539	35.53/0.9783	31.49/0.9580	35.01/0.9745	34.35/0.9711
NNM	36.49/0.9768	39.70/0.9807	26.99/0.9568	33.72/0.9764	30.08/0.9441	32.51/0.9620	33.25/0.9662
NCW-NNM	39.39/0.9855	40.93/0.984	28.67/0.971	38.39/0.9887	31.94/0.9637	36.09/0.9785	35.90/0.9786

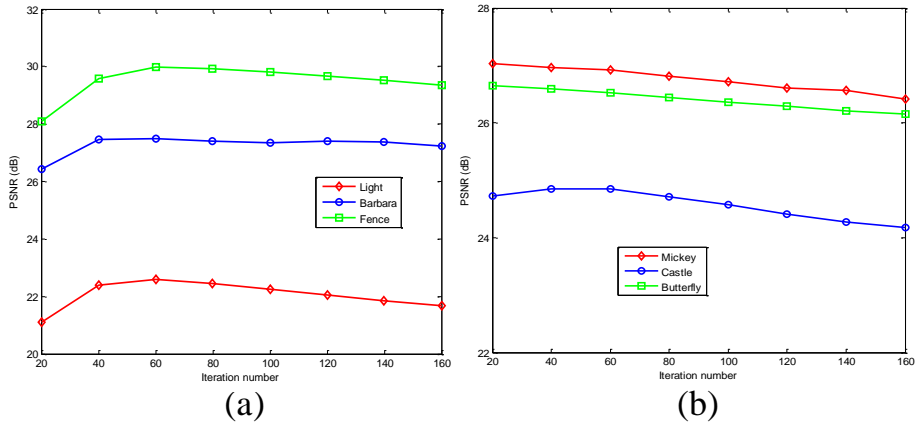


Figure 9: Performance comparison with different matched patch numbers m for image deblurring and image inpainting. (a) PSNR results achieved by different k in the case of 9×9 Uniform Kernel, $\delta = \sqrt{2}$. (b) PSNR results achieved by different k in the case of the image inpainting with 80% missing sample.

245 cally, to investigate the sensitivity of our method against m , two experiments are conducted with respect to different m , ranging from 20 to 160, in the case of image deblurring and image inpainting, respectively. The results with different m are shown in Fig. 9. It can be seen that all the curves are almost flat, showing the performance of the proposed NCW-NNM is insensitive to m . The best performance of each case is usually achieved with m in the range [40,80].
 250 Therefore, in this work m is empirically set to be 60.

4.5. Comparison of NNM method

In this subsection, to demonstrate the proposed NCW-NNM can improve the accuracy of the rank approximation effectively, we compare it with traditional nuclear norm minimization (NNM) method. In terms of the quantitative
 255 metrics, one can observe that the PSNR and FSIM results of the NNM and the proposed NCW-NNM methods for image deblurring, image inpainting and image CS recovery are shown in Table 2, Table 3 and Table 4, respectively. It can be seen that NCW-NNM consistently outperforms the NNM method based

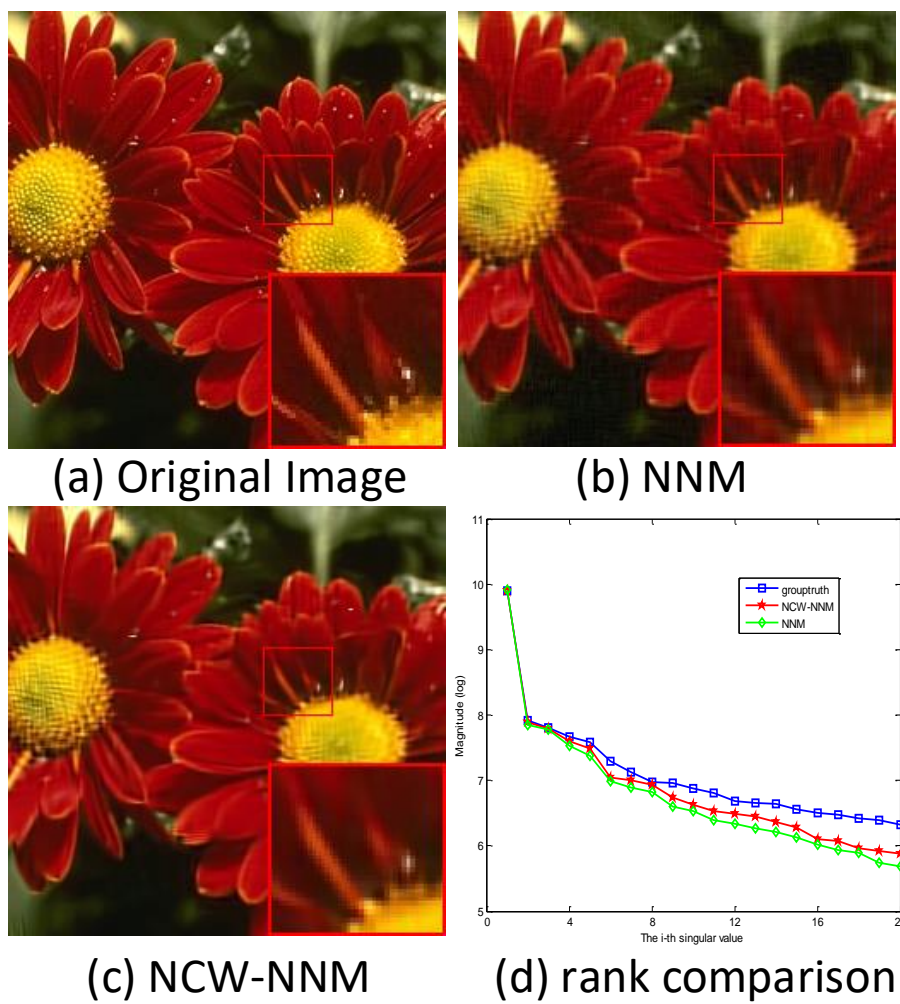


Figure 10: Deblurring performance comparison on the *Flower* image with 19×19 uniform blur, $\delta = \sqrt{2}$. (a) Original image; deblurred image by (b) NNM (PSNR = 28.91dB, FSIM = 0.8875); (c) NCW-NNM (PSNR = **29.27dB**, FSIM = **0.9043**); (d) Comparison the rank of NNM and NCW-NNM methods.

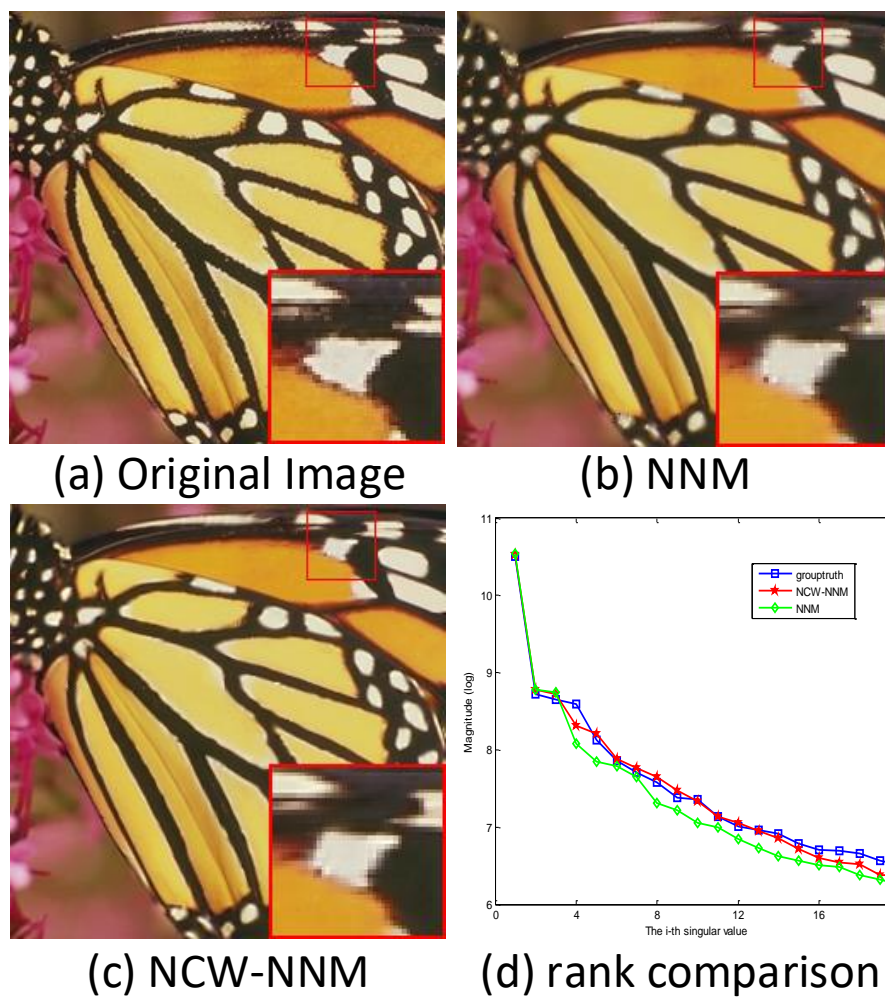


Figure 11: Visual comparison of *Butterfly* by image inpainting with 80% pixels missing. (a) Original image; (b) Degraded image with 80% missing sample; deblurred image by (c) NNM (PSNR = 25.61dB, FSIM = 0.9125); (d) NCW-NNM (PSNR = **26.52dB**, FSIM = **0.9271**); (e) Comparison the rank of NNM and NCW-NNM methods.

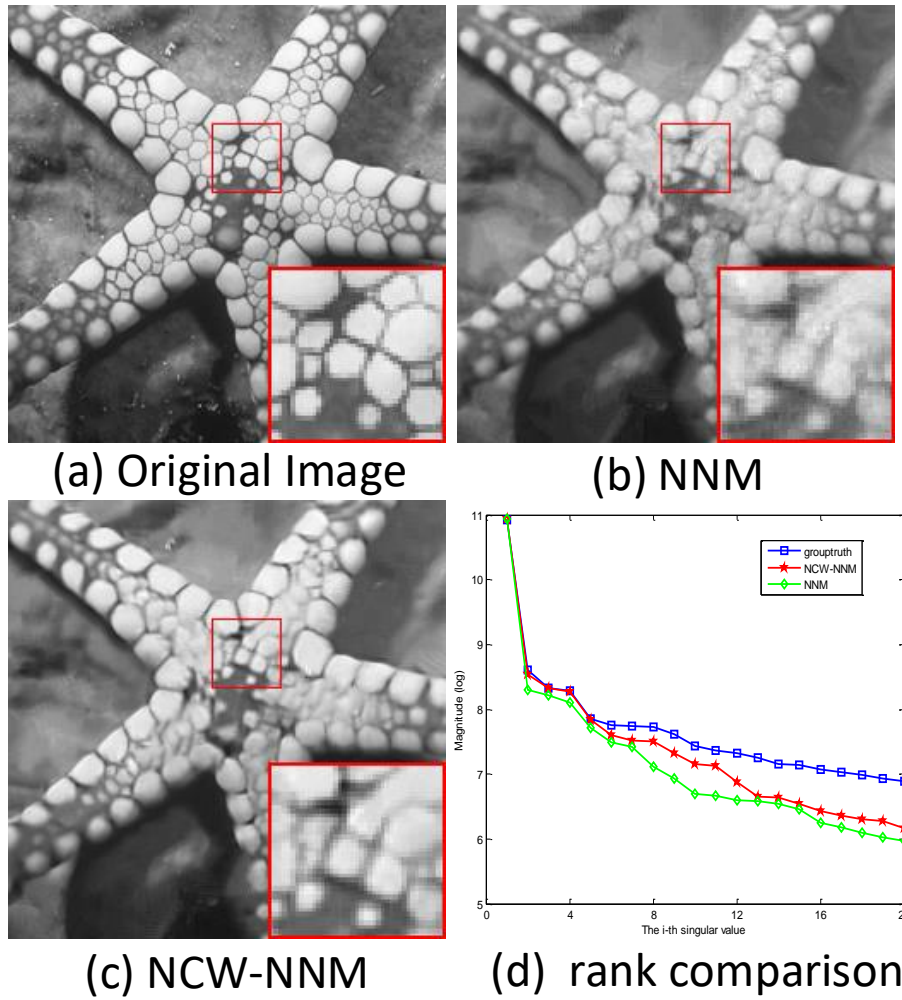


Figure 12: Visual comparison of *Leaves* by image CS recovery with $0.1N$ measurements. (a) Original image; (b) NNM (PSNR = 24.21dB, FSIM = 0.8484); (c) NCW-NNM (PSNR = 25.49dB, FSIM = 0.8755); (d) Comparison the rank of NNM and NCW-NNM methods.

260 on all IR tasks. The visual comparison results of image deblurring, image in-
 265 painting and image CS recovery are shown in Fig. 10, Fig. 11 and Fig. 12,
 respectively. It can be seen that the proposed NCW-NNM produces much clear
 and better visual results than NNM method.

Moreover, Fig. 10 (d), Fig. 11 (d) and Fig. 12 (d) show the singular values of
 265 these two rank approximation methods, respectively, where the data matrices
 are generated by selecting 60 similar image patches in accordance with the
 small red square exemplar patch. It can be seen that the singular values of
 the proposed NCW-NNM result is the best approximation to the grouptruth
 in comparison with NNM method. Therefore, the proposed NCW-NNM can
 270 enforce more accurate rank approximation results than NNM method. The
 main reason is that NNM method tends to over-shrink the rank components and
 treats each rank component equally, which cannot obtain the approximation of
 the matrix rank accurately. Different from NNM method, the proposed NNW-
 NNM assigns the different weight to each singular value and avoids the over-
 275 shrink phenomena. Accordingly, the proposed NCW-NNM can obtain more
 accurate rank approximation results than NNM method.

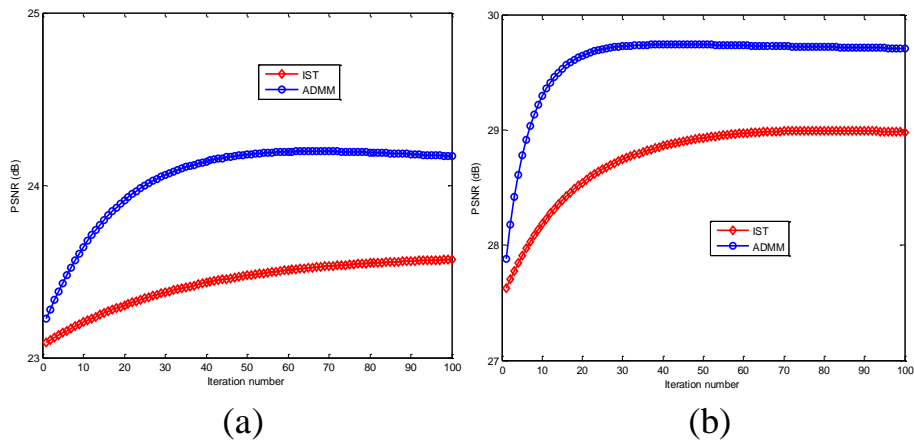


Figure 13: Comparison between ADMM and IST. (a) PSNR results achieved by ADMM and IST with ratio =0.2 for image *fingerprint*. (b) PSNR results achieved by ADMM and IST with ratio =0.3 for image *pentagon*.

4.6. Comparison Between ADMM and IST

In this subsection, the classical optimization method: iterative shrinkage/theresholding (IST) [69] is used to solve our proposed non-convex model for CS image reconstruction. We will make a comparison between ADMM and IST with ratio = 0.2 and ratio= 0.3 for two image *fingerprint* and *pentagon* as examples, respectively. Fig. 13 shows the progression curves of the PSNR (dB) results achieved by ADMM and IST, respectively. It can be seen that ADMM algorithm is more fast efficient and effective to solve the proposed non-convex model than traditional IST algorithm.

4.7. Convergence

Since the proposed model is non-convex, it is difficult to give its theoretical proof for global convergence. Here, we only provide empirical evidence to display the good convergence of the proposed NCW-NNM method. Fig. 14 illustrates the convergent performance of the proposed NCW-NNM. It shows the curves of the PSNR values versus the iteration numbers for image deblurring with 9×9 Uniform Kernel, $\delta = \sqrt{2}$ as well as image inpainting with 80% pixels missing, respectively. One can observe that with the increase of the iteration numbers, the PSNR curves gradually increase and ultimately become flat and stable, and thus exhibiting the good stability of the proposed NCW-NNM method.

5. Conclusion

Image priors based on nonlocal self-similarity (NSS) and low-rank matrix approximation (LRMA) have achieved a great success in image restoration. However, since the singular values have clear meanings and should be treated differently, traditional nuclear norm minimization (NNM) regularized each of them equally, which often restricted its capability and flexibility. To rectify the

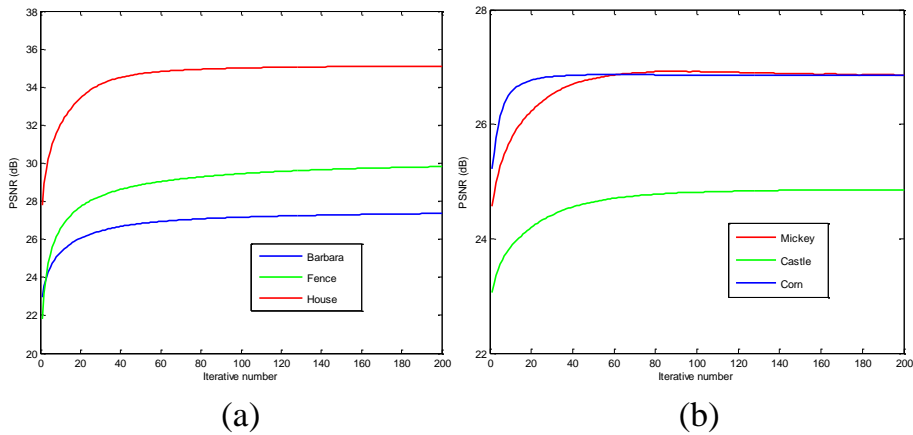


Figure 14: Convergence analysis of the proposed approach. (a) PSNR results versus iteration number for image deblurring with 9×9 Uniform Kernel, $\delta = \sqrt{2}$. (b) PSNR results versus iteration number for image inpainting with 80% pixels missing.

shortcoming of the nuclear norm, this paper proposed a new method for image restoration via non-convex weighted ℓ_p nuclear norm minimization (NCW-NNM). To make the optimization tractable, the alternative direction multiplier method (ADMM) framework was used to solve the proposed non-convex model.

305 Experimental results on three image restoration applications, image deblurring, image inpainting and image CS recovery, have shown that the proposed method outperforms many current state-of-the-art methods both quantitatively and qualitatively.

References

310 **References**

- [1] Buades A, Coll B, Morel J M. A non-local algorithm for image denoising[C]//Computer Vision and Pattern Recognition, 2005. CVPR 2005. IEEE Computer Society Conference on. IEEE, 2005, 2: 60-65.
- [2] Li B, Xie W. Image denoising and enhancement based on adaptive fractional calculus of small probability strategy[J]. Neurocomputing, 2016, 175: 704-714.

315

- [3] Mairal J, Bach F, Ponce J, et al. Non-local sparse models for image restoration[C]//Computer Vision, 2009 IEEE 12th International Conference on. IEEE, 2009: 2272-2279.
- [4] Gu S, Zhang L, Zuo W, et al. Weighted nuclear norm minimization with application to image denoising[C]//Proceedings of the IEEE Conference on Computer Vision and Pattern Recognition. 2014: 2862-2869.
- [5] Song C, Deng H, Gao H, et al. Bayesian non-parametric gradient histogram estimation for texture-enhanced image deblurring[J]. Neurocomputing, 2016, 197: 95-112.
- [6] Huang C, Ding X, Fang C, et al. Robust image restoration via adaptive low-rank approximation and joint kernel regression[J]. IEEE Transactions on Image Processing, 2014, 23(12): 5284-5297.
- [7] Zhang J, Zhao D, Xiong R, et al. Image restoration using joint statistical modeling in a space-transform domain[J]. IEEE Transactions on Circuits and Systems for Video Technology, 2014, 24(6): 915-928.
- [8] Deng X, Shen Y, Song M, et al. Video-based non-uniform object motion blur estimation and deblurring[J]. Neurocomputing, 2012, 86: 170-178.
- [9] Jin K H, Ye J C. Annihilating filter-based low-rank Hankel matrix approach for image inpainting[J]. IEEE Transactions on Image Processing, 2015, 24(11): 3498-3511.
- [10] Zhou M, Chen H, Paisley J, et al. Nonparametric Bayesian dictionary learning for analysis of noisy and incomplete images[J]. IEEE Transactions on Image Processing, 2012, 21(1): 130-144.
- [11] Wang J, Lu K, Pan D, et al. Robust object removal with an exemplar-based image inpainting approach[J]. Neurocomputing, 2014, 123: 150-155.
- [12] Chen D Q, Zhou Y. Inexact alternating direction method based on proximity projection operator for image inpainting in wavelet domain[J]. Neurocomputing, 2016, 189: 145-159.

- [13] Shen Y, Li J, Zhu Z, et al. Image reconstruction algorithm from compressed sensing measurements by dictionary learning[J]. Neurocomputing, 2015, 151: 1153-1162.
- [14] Zhang J, Zhao D, Zhao C, et al. Image compressive sensing recovery via collaborative sparsity[J]. IEEE Journal on Emerging and Selected Topics in Circuits and Systems, 2012, 2(3): 380-391.
- [15] Dong W, Shi G, Li X, et al. Image reconstruction with locally adaptive sparsity and nonlocal robust regularization[J]. Signal Processing: Image Communication, 2012, 27(10): 1109-1122.
- [16] Zha Z, Liu X, Zhang X, et al. Compressed sensing image reconstruction via adaptive sparse nonlocal regularization[J]. The Visual Computer, 2016: 1-21.
- [17] Engl H W, Kunisch K, Neubauer A. Convergence rates for Tikhonov regularization of non-linear ill-posed problems[J]. Inverse problems, 1989, 5(4): 523.
- [18] Rudin L I, Osher S, Fatemi E. Nonlinear total variation based noise removal algorithms[J]. Physica D: Nonlinear Phenomena, 1992, 60(1-4): 259-268.
- [19] Chambolle A. An algorithm for total variation minimization and applications[J]. Journal of Mathematical imaging and vision, 2004, 20(1): 89-97.
- [20] Aharon M, Elad M, Bruckstein A. *rmk*-SVD: An algorithm for designing overcomplete dictionaries for sparse representation[J]. IEEE Transactions on signal processing, 2006, 54(11): 4311-4322.
- [21] Elad M, Aharon M. Image denoising via sparse and redundant representations over learned dictionaries[J]. IEEE Transactions on Image processing, 2006, 15(12): 3736-3745.
- [22] Dong W, Zhang L, Shi G, et al. Image deblurring and super-resolution by adaptive sparse domain selection and adaptive regularization[J]. IEEE Transactions on Image Processing, 2011, 20(7): 1838-1857.
- [23] Zhang J, Zhao C, Zhao D, et al. Image compressive sensing recovery using adaptively learned sparsifying basis via L0 minimization[J]. Signal Processing, 2014, 103: 114-126.

- [24] Mairal J, Bach F, Ponce J, et al. Online dictionary learning for sparse coding[C]//Proceedings of the 26th annual international conference on machine learning. ACM, 2009: 689-696.
375
- [25] Mairal J, Bach F, Ponce J. Task-driven dictionary learning[J]. IEEE transactions on pattern analysis and machine intelligence, 2012, 34(4): 791-804.
- [26] Dong W, Zhang L, Shi G, et al. Nonlocally centralized sparse representation for image restoration[J]. IEEE Transactions on Image Processing, 2013, 22(4): 1620-1630.
380
- [27] Zhang X, Burger M, Bresson X, et al. Bregmanized nonlocal regularization for deconvolution and sparse reconstruction[J]. SIAM Journal on Imaging Sciences, 2010, 3(3): 253-276.
- [28] Dabov K, Foi A, Katkovnik V, et al. Image denoising by sparse 3-D transform-domain collaborative filtering[J]. IEEE Transactions on image processing, 2007, 16(8): 2080-2095.
385
- [29] Zhang J, Zhao D, Gao W. Group-based sparse representation for image restoration[J]. IEEE Transactions on Image Processing, 2014, 23(8): 3336-3351.
- [30] Zha Z, Liu X, Zhou Z, et al. Image denoising via group sparsity residual constraint[C]//Acoustics, Speech and Signal Processing (ICASSP), 2017 IEEE International Conference on. IEEE, 2017: 1787-1791.
390
- [31] Fazel M. Matrix rank minimization with applications[D]. PhD thesis, Stanford University, 2002.
- [32] Kang Z, Peng C, Cheng Q. Robust PCA via nonconvex rank approximation[C]//Data Mining (ICDM), 2015 IEEE International Conference on. IEEE, 2015: 211-220.
395
- [33] Candes E, Recht B. Exact matrix completion via convex optimization[J]. Communications of the ACM, 2012, 55(6): 111-119.
- [34] Peng C, Kang Z, Li H, et al. Subspace clustering using log-determinant rank approximation[C]//Proceedings of the 21th ACM SIGKDD International Conference on Knowledge Discovery and Data Mining. ACM, 2015: 925-934.
400

- [35] Peng Y, Ganesh A, Wright J, et al. RASL: Robust alignment by sparse and low-rank decomposition for linearly correlated images[J]. IEEE Transactions on Pattern Analysis and Machine Intelligence, 2012, 34(11): 2233-2246.
- 405 [36] Dong W, Shi G, Li X. Nonlocal image restoration with bilateral variance estimation: A low-rank approach[J]. IEEE transactions on image processing, 2013, 22(2): 700-711.
- [37] Zhang J, Xiong R, Zhao C, et al. CONCOLOR: Constrained non-convex low-rank model for image deblurring[J]. IEEE Transactions on Image Processing, 410 2016, 25(3): 1246-1259.
- [38] Ji H, Liu C, Shen Z, et al. Robust video denoising using low rank matrix completion[C]//Computer Vision and Pattern Recognition (CVPR), 2010 IEEE Conference on. IEEE, 2010: 1791-1798.
- [39] Xie Y, Gu S, Liu Y, et al. Weighted Schatten p -norm minimization for image 415 denoising and background subtraction[J]. IEEE transactions on image processing, 2016, 25(10): 4842-4857.
- [40] Pan J, Liu R, Su Z, et al. Motion blur kernel estimation via salient edges and low rank prior[C]//Multimedia and Expo (ICME), 2014 IEEE International Conference on. IEEE, 2014: 1-6.
- 420 [41] Dong W, Shi G, Li X. Image deblurring with low-rank approximation structured sparse representation[C]//Signal & Information Processing Association Annual Summit and Conference (APSIPA ASC), 2012 Asia-Pacific. IEEE, 2012: 1-5.
- [42] Li M, Liu J, Xiong Z, et al. MARLow: A Joint Multiplanar Autoregressive and Low-Rank Approach for Image Completion[C]//European Conference on Computer Vision. Springer International Publishing, 2016: 819-834. 425
- [43] Cai J F, Cands E J, Shen Z. A singular value thresholding algorithm for matrix completion[J]. SIAM Journal on Optimization, 2010, 20(4): 1956-1982.
- [44] Chartrand R, Wohlberg B. A nonconvex ADMM algorithm for group sparsity with sparse groups[C]//Acoustics, Speech and Signal Processing (ICASSP), 2013 430 IEEE International Conference on. IEEE, 2013: 6009-6013.

- [45] Zuo W, Meng D, Zhang L, et al. A generalized iterated shrinkage algorithm for non-convex sparse coding[C]//Proceedings of the IEEE international conference on computer vision. 2013: 217-224.
- [46] Lyu Q, Lin Z, She Y, et al. A comparison of typical ℓ_p minimization algorithms[J]. Neurocomputing, 2013, 119: 413-424.
- [47] Nie F, Huang H, Ding C H Q. Low-Rank Matrix Recovery via Efficient Schatten p -Norm Minimization[C]//AAAI. 2012.
- [48] Liu L, Huang W, Chen D R. Exact minimum rank approximation via Schatten p -norm minimization[J]. Journal of Computational and Applied Mathematics, 2014, 267: 218-227.
- [49] Nie F, Wang H, Huang H, et al. Joint Schatten p -norm and ℓ_p -norm robust matrix completion for missing value recovery[J]. Knowledge and Information Systems, 2015, 42(3): 525-544.
- [50] Zha Z, Liu X, Huang X, et al. Analyzing the group sparsity based on the rank minimization methods[J]. arXiv preprint arXiv:1611.08983, 2016.
- [51] Candes E J, Wakin M B, Boyd S P. Enhancing sparsity by reweighted ℓ_1 minimization[J]. Journal of Fourier analysis and applications, 2008, 14(5): 877-905.
- [52] Boyd S, Parikh N, Chu E, et al. Distributed optimization and statistical learning via the alternating direction method of multipliers[J]. Foundations and Trends in Machine Learning, 2011, 3(1): 1-122.
- [53] Zhao C, Zhang J, Ma S, et al. Nonconvex L_p nuclear norm based ADMM framework for compressed sensing[C]//Data Compression Conference (DCC), 2016. IEEE, 2016: 161-170.
- [54] Dong W, Shi G, Li X, et al. Compressive sensing via nonlocal low-rank regularization[J]. IEEE Transactions on Image Processing, 2014, 23(8): 3618-3632.
- [55] Afonso M V, Bioucas-Dias J M, Figueiredo M A T. Fast image recovery using variable splitting and constrained optimization[J]. IEEE Transactions on Image Processing, 2010, 19(9): 2345-2356.

- 460 [56] Avriel M. Nonlinear programming: analysis and methods[M]. Courier Corporation, 2003.
- [57] Chang S G, Yu B, Vetterli M. Adaptive wavelet thresholding for image denoising and compression[J]. IEEE transactions on image processing, 2000, 9(9): 1532-1546.
- 465 [58] Zhang L, Zhang L, Mou X, et al. FSIM: A feature similarity index for image quality assessment[J]. IEEE transactions on Image Processing, 2011, 20(8): 2378-2386.
- [59] Dabov K, Foi A, Katkovnik V, et al. Image restoration by sparse 3D transform-domain collaborative filtering[C]//Image Processing: Algorithms and Systems. 2008: 681207.
- 470 [60] Pappyan V, Elad M. Multi-scale patch-based image restoration[J]. IEEE Transactions on image processing, 2016, 25(1): 249-261.
- [61] Xu Y, Yin W. A fast patch-dictionary method for whole image recovery[J]. arXiv preprint arXiv:1408.3740, 2014.
- 475 [62] Takeda H, Farsiu S, Milanfar P. Deblurring using regularized locally adaptive kernel regression[J]. IEEE transactions on image processing, 2008, 17(4): 550-563.
- [63] Afonso M V, Bioucas-Dias J M, Figueiredo M A T. An augmented Lagrangian approach to the constrained optimization formulation of imaging inverse problems[J]. IEEE Transactions on Image Processing, 2011, 20(3): 681-695.
- 480 [64] Ram I, Elad M, Cohen I. Image processing using smooth ordering of its patches[J]. IEEE transactions on image processing, 2013, 22(7): 2764-2774.
- [65] Mun S, Fowler J E. Block compressed sensing of images using directional transforms[C]//Image Processing (ICIP), 2009 16th IEEE International Conference on. IEEE, 2009: 3021-3024.
- 485 [66] Egiazarian K, Foi A, Katkovnik V. Compressed sensing image reconstruction via recursive spatially adaptive filtering[C]//Image Processing, 2007. ICIP 2007. IEEE International Conference on. IEEE, 2007, 1: I-549-I-552.

- [67] Zhang J, Zhao D, Jiang F, et al. Structural group sparse representation for image compressive sensing recovery[C]//Data Compression Conference (DCC), 2013. IEEE, 2013: 331-340.
- [68] Canh T N, Dinh K Q, Jeon B. Multi-scale/multi-resolution Kronecker compressive imaging[C]//Image Processing (ICIP), 2015 IEEE International Conference on. IEEE, 2015: 2700-2704.
- [69] Beck A, Teboulle M. Fast gradient-based algorithms for constrained total variation image denoising and deblurring problems[J]. IEEE Transactions on Image Processing, 2009, 18(11): 2419-2434.
- [70] Chen C L P, Liu L, Chen L, et al. Weighted couple sparse representation with classified regularization for impulse noise removal[J]. IEEE Transactions on Image Processing, 2015, 24(11): 4014-4026.
- [71] Mirsky L. A trace inequality of John von Neumann[J]. Monatshefte für Mathematik, 1975, 79(4): 303-306.